

# Rotating atomic quantum gases with light-induced azimuthal gauge potentials and the observation of the Hess-Fairbank effect

P. -K. Chen,<sup>1</sup> L. -R. Liu,<sup>1</sup> M. -J. Tsai,<sup>1</sup> N. -C. Chiu,<sup>1</sup> Y. Kawaguchi,<sup>2</sup> S. -K. Yip,<sup>1,3</sup> M. -S. Chang,<sup>1</sup> and Y. -J. Lin<sup>1,\*</sup>

<sup>1</sup>*Institute of Atomic and Molecular Sciences, Academia Sinica, Taipei, Taiwan 10617*

<sup>2</sup>*Department of Applied Physics, Nagoya University, Nagoya, 464-8603, Japan*

<sup>3</sup>*Institute of Physics, Academia Sinica, Taipei, Taiwan 11529*

(Dated: December 18, 2018)

We demonstrate synthetic azimuthal gauge potentials for Bose-Einstein condensates from engineering atom-light couplings. The gauge potential is created by adiabatically loading the condensate into the lowest energy Raman-dressed state, achieving a coreless vortex state. The azimuthal gauge potentials act as effective rotations and are tunable by the Raman coupling and detuning. We characterize the spin textures of the dressed states, in agreements with the theory. The lowest energy dressed state is stable with a 4.5-s half-atom-number-fraction lifetime. In addition, we exploit the azimuthal gauge potential to demonstrate the Hess-Fairbank effect, the analogue of Meissner effect in superconductors. The atoms in the absolute ground state has a zero quasi-angular momentum and transits into a polar-core vortex when the synthetic magnetic flux is tuned to exceed a critical value. Our demonstration serves as a paradigm to create topological excitations by tailoring atom-light interactions where both types of SO(3) vortices in the  $|\langle \vec{F} \rangle| = 1$  manifold, coreless vortices and polar-core vortices, are created in our experiment. The gauge field in the stationary Hamiltonian opens a path to investigating rotation properties of atomic superfluids under thermal equilibrium.

Synthetic gauge fields for ultracold neutral atoms [1–9] marked one of the milestones toward creating topological quantum matters and exploring novel quantum phenomenon. Among various implementations, the optical Raman coupling scheme is to couple different internal spin states while transferring photon momentum. This leads to the spin-linear-momentum coupling [8–12], which is a type of “general spin-orbit-coupling” (SOC), referring to coupling between the atomic spin and the center-of-mass motion of the atoms. Another class of SOC where the atomic spin is coupled to the orbital-angular-momentum (OAM) of the atoms [13], has been demonstrated using one Laguerre-Gaussian (LG) Raman beam carrying OAM of light [14]; this is the spin-orbital-angular-momentum coupling (SOAMC) [15–18].

In SOAMC systems, the atoms dressed by LG Raman beams experience azimuthal gauge potentials  $\vec{A} = A(r)\mathbf{e}_\phi$ , where the azimuthal dispersion is  $(\ell - \ell_{\min})^2/2mr^2$  at radial position  $r$  and  $\ell$  is the angular momentum. The shifted minimum is  $\ell_{\min} = rA(r)$ , where  $A(r)$  is tunable by the Raman coupling strength  $\Omega(r)$  and Raman detuning  $\delta$  in our experiment. This azimuthal gauge potential is thus equivalent to an effective rotation in the stationary Hamiltonian. Rotating atomic quantum gases with such azimuthal gauge potentials differs from those where metastable superflows are created by resonant pulses of Raman LG beams [19, 20] or mechanical stirring [21]. In such cases the spinor wave function is not the eigenstate of the Hamiltonian, therefore the gauge potential is not well defined. Differing from applying Raman pulses in the Rabi-flopping regime, one typically prepares dressed eigenstates with gauge potentials by adiabatically sweeping the detuning (see later text).

The light-induced azimuthal gauge potential can in

principle be used to measure superfluid fractions from the spin population imbalance [22]. Superfluid fraction corresponds to a nonclassical rotational inertia (NCRI) [23, 24], which is a property of systems under thermal equilibrium, rather than of metastable systems. In Refs. [23, 24], NCRI is manifested in the Hess-Fairbank effect [25, 26]: with a cylindrical container filled with  ${}^4\text{He}$  rotates at a sufficiently low speed, after  ${}^4\text{He}$  is cooled below the superfluid transition temperature, the atoms stop rotating and become out-of-equilibrium with the container. NCRI is also an analog of the Meissner effect in superconductors [23, 24].

Some attempts have been made to realize light-induced azimuthal gauge potentials. In Ref. [27], Bose-Einstein condensates (BECs) in a ring trap under LG Raman beams with the OAM transfer between spin states ( $|m_F\rangle \rightarrow |m_F + 1\rangle$ )  $\Delta\ell = 3\hbar$  are studied; a lifetime of  $\sim 0.1$  s of the lowest energy dressed state atoms is reported.  $F = 1$  SOAMC BECs are demonstrated in Ref. [14] with the gauge potential  $A = 0$ , given that the atoms are in the middle-energy dressed state in the  $\langle \vec{F} \rangle = 0$  polar phase. In this paper, we present the first experimental realization of such azimuthal gauge potential ( $A \neq 0$ ) with SOAMC BECs in the lowest energy dressed state.

SOAMC BECs can be implemented with an atom-light coupling  $\vec{\Omega}_{\text{eff}} \cdot \vec{F}$  where the direction of  $\vec{\Omega}_{\text{eff}}$  winds by a multiple of  $2\pi$  as the azimuthal angle  $\phi$  increases from 0 to  $2\pi$ . Here,  $\vec{\Omega}_{\text{eff}}$  is a light-induced effective magnetic field [8] typically realized by LG Raman beams [14] and  $\vec{F}$  is the atomic spin. Topological excitations in spinor BECs, where the rich variety of order parameters accommodates various types of topological defects [28, 29], can be created by versatile design of  $\vec{\Omega}_{\text{eff}}$ . This is analo-

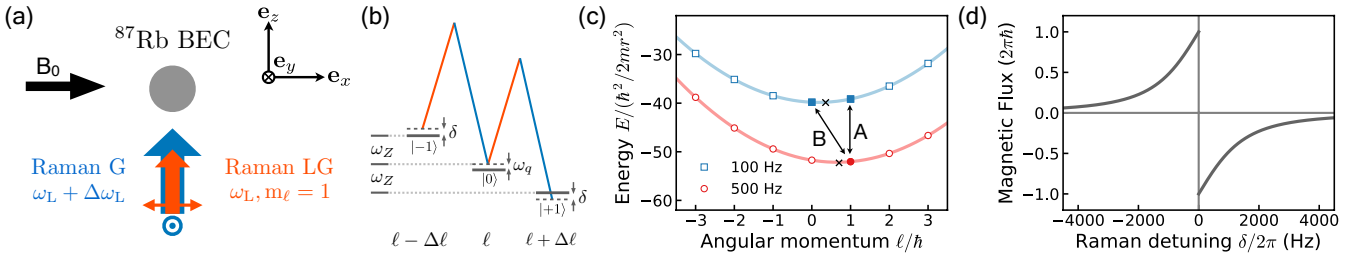


FIG. 1: Experimental schematic and properties of the dressed state. (a) Experiment setup (b) Level diagram in  $F = 1$  manifold (c) Energy dispersion versus quasi-angular momentum  $\ell$  at  $r = 2.0 \mu\text{m}$  for  $\delta/2\pi = 100$  and  $500 \text{ Hz}$ . “A” indicates  $\ell = \hbar$  for both detunings in Fig. 2 data and “B” indicates  $\ell_g = 0, \hbar$  for  $\delta/2\pi = 100$  and  $500 \text{ Hz}$  in Fig. 4, respectively. The x-marks indicate the minimum. (d) Synthetic magnetic flux  $\Phi_{B^*}^\pm$  enclosed by the condensate radius  $R$  versus  $\delta/2\pi$ .

gous to the works using spin rotation with real magnetic fields  $\vec{B}$  with the Hamiltonian term  $\vec{B} \cdot \vec{F}$  [30], where coreless vortices [31], monopoles [32–35], 2D [36, 37] and 3D skyrmions [38], and the geometric Hall effect [39] are demonstrated. Furthermore, 2D skyrmions [40] and spin monopoles [41] with pulses of Raman LG beams are achieved.

In this letter, we first load a BEC into the lowest energy Raman-dressed state, creating a coreless vortex [28]. Here one Raman beam is LG and carries OAM. The dressed atoms experience azimuthal gauge potentials as effective rotations, which we exploit to demonstrate the Hess-Fairbank effect. As the synthetic magnetic flux arising from the effective rotation is below a critical value, the dressed atoms in the absolute ground state in the thermal equilibrium have zero quasi-angular momentum  $\ell^\pm$  (see later texts and Eq. (4)), being a coreless vortex. Above the critical flux, a polar-core vortex [28, 42, 43] with nonzero  $\ell^\pm = \mp\hbar$  is achieved. We demonstrate the capability to create both types of SO(3) vortices [28, 29], the  $\mathbb{Z}_2 = 0$  coreless vortex and  $\mathbb{Z}_2 = 1$  polar-core vortex (see the schematic drawing in Fig. 4b), in a unified and controlled scheme. This opens a path for creating topological excitations by tailoring atom-light interactions.

For atoms under sufficiently large  $\vec{\Omega}_{\text{eff}} \cdot \vec{F}$  such that the motional kinetic energy  $-(\hbar^2/2m)\nabla^2$  is negligible, the energy eigenstates of the overall Hamiltonian are well approximated by the eigenstates  $|\xi_n\rangle$  of  $\vec{\Omega}_{\text{eff}} \cdot \vec{F}$ . Under this approximation, the atom’s spinor wave function follows the local dressed eigenstate  $|\xi_n\rangle$ , whose quantization axis is along  $\vec{\Omega}_{\text{eff}} = \Omega(r) \cos \phi \mathbf{e}_x - \Omega(r) \sin \phi \mathbf{e}_y + \delta \mathbf{e}_z$  given by our Raman beams. The state of dressed atoms is  $\langle \vec{r} | \Psi \rangle = \varphi_n(\vec{r}) |\xi_n(\vec{r})\rangle$ , where  $\varphi_n$  is the external part and  $|\xi_n\rangle$  is the normalized spin part of the wave function.  $|\varphi_n| = \sqrt{n_a}$  where  $n_a$  is the density. The effective Hamiltonian for atoms projected to  $|\xi_n\rangle$ , which governs the evolution of  $\varphi_n$ , is [14]

$$H_{\text{eff}}^{(n)} = \frac{-\hbar^2}{2m} \nabla^2(r, z) + \frac{(L_z - rA_n)^2}{2mr^2} + V(r) + \varepsilon_n + W_n. \quad (1)$$

Here  $L_z = -i\hbar\partial_\phi$  is the angular momentum operator for  $\varphi_n$  with the eigenvalue  $\ell$ , and  $A_n(r) = (i\hbar/r)\langle \xi_n | \partial_\phi \xi_n \rangle$

is the azimuthal gauge potential.  $V(r)$  is the spin-independent trap,  $\varepsilon_n = n\sqrt{\Omega(r)^2 + \delta^2}$  is the eigenenergy of  $\vec{\Omega}_{\text{eff}} \cdot \vec{F}$ , and  $W_n \approx \hbar^2/2mr^2$  is the geometric scalar potential. We label the lowest, middle, and highest energy dressed states as  $|\xi_{-1}\rangle, |\xi_0\rangle, |\xi_1\rangle$ , respectively.  $|\xi_{-1}\rangle$  is given by Euler rotations [44]

$$|\xi_{-1}\rangle = e^{i(\theta+\gamma)} \left( e^{i\phi \frac{1-\cos\beta}{2}}, -\frac{\sin\beta}{\sqrt{2}}, e^{-i\phi \frac{1+\cos\beta}{2}} \right)^T, \quad (2)$$

where  $\beta(r) = \tan^{-1}[\Omega(r)/\delta]$  is the polar angle of  $\vec{\Omega}_{\text{eff}}$ , and  $\theta + \gamma$  is the phase from a gauge transformation. By choosing  $\theta + \gamma = 0$  for all  $\delta$ , it leads to

$$A_{-1} = (\hbar/r) \cos \beta, \quad (3)$$

where the angular momentum of  $\varphi_{-1}$  is  $\ell$  in this gauge, and  $\ell, \ell \pm \hbar$  are the mechanical angular momenta of the bare spin  $|m_F = 0, \pm 1\rangle$  components of the state  $\varphi_{-1}|\xi_{-1}\rangle$ , respectively. In order to avoid a singularity at  $r = 0$  in the synthetic magnetic field  $\vec{B}^* = \nabla \times \vec{A}$  [45] as  $A_{-1}(r \rightarrow 0) \rightarrow \pm \hbar/r$  for  $\delta > (<)0$ , we use alternative gauges with  $\theta + \gamma = \pm\phi$ , leading to

$$A_{-1}^\pm = \frac{\hbar}{r} (\cos \beta \mp 1), \ell^\pm = \ell \mp \hbar \quad (4)$$

for  $\delta > (<)0$ , where  $\ell^\pm$  is the angular momentum of the external wave function  $\varphi_{-1}^\pm$  in these gauges. Note that the mechanical angular momentum  $\ell - rA_{-1} = \ell^\pm - rA_{-1}^\pm$  is gauge invariant.

Consider atoms in the lowest energy dressed state  $|\xi_{-1}\rangle$  prepared by loading a ground state BEC in  $|m_F = -1\rangle$  with a Thomas-Fermi (TF) wave function  $\varphi_{\text{TF}} = \sqrt{n_{\text{TF}}}$ , where  $\langle \vec{r} | \Psi \rangle_{t=0} = \varphi_{\text{TF}}(0, 0, 1)^T$ . The atoms are loaded to  $|\xi_{-1}\rangle$  as

$$\langle \vec{r} | \Psi \rangle = \varphi_{\text{TF}} \left( e^{i2\phi \frac{1-\cos\beta}{2}}, -e^{i\phi \frac{\sin\beta}{\sqrt{2}}}, \frac{1+\cos\beta}{2} \right)^T, \quad (5)$$

where the phase winding of the  $m_F = -1$  component remains zero during loading, and the potential  $V(r)$  is cylindrically symmetric. Eq. (5) has  $\ell = \hbar$  using the gauge in Eq. (3), as shown in our data in Fig. 2. The

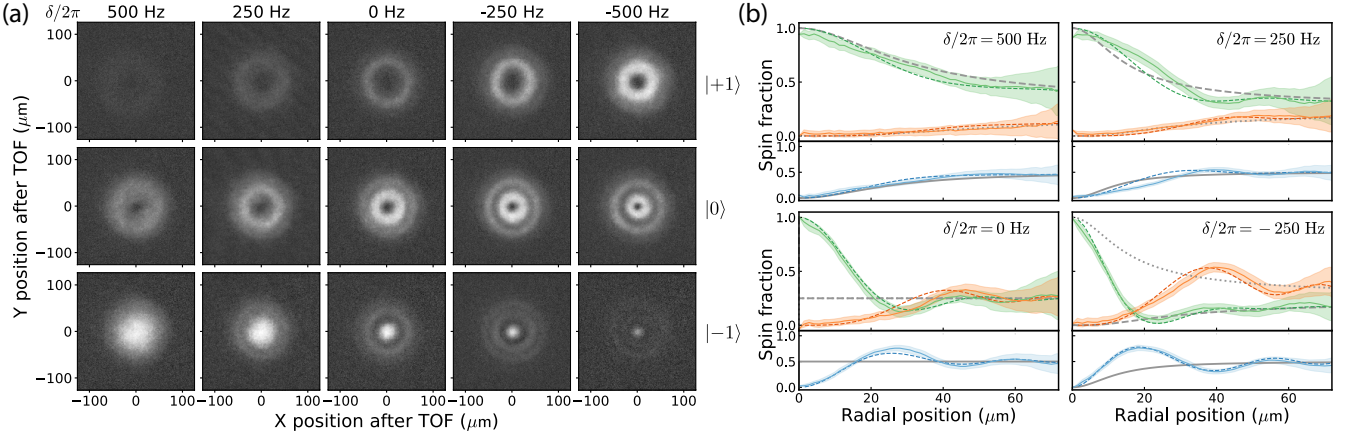


FIG. 2: (a) Absorption images  $D_{m_F}$  of the lowest energy dressed state projected onto bare spin  $|m_F\rangle$  states with various detuning  $\delta$  after 24 ms TOF. (b) Experimental spin fractions (solid colored lines) versus the radial position are compared to the spin texture from  $|\xi_{-1}\rangle$  (gray lines) and the TOF simulations from TDGPE (dashed colored lines). The green, orange and blue curves represents the  $|-1\rangle$ ,  $|1\rangle$ ,  $|0\rangle$  components, respectively, where the shaded area indicates the standard deviation along  $\mathbf{e}_\phi$ . The in-situ spin textures Eq. (5) after a magnification of  $r \rightarrow r/13.0$  after TOF [14, 46] are shown as gray-dashed, -dotted, -solid lines for  $|-1\rangle$ ,  $|1\rangle$ ,  $|0\rangle$  states.

atom's spinor wave function follows  $|\xi_{-1}\rangle$  only at  $r \gtrsim r_c$  due to the vanishing intensity of LG beam at  $r = 0$ , where  $r_c$  is the adiabatic radius. At  $r \gtrsim r_c$ , the radial kinetic energy is negligible and for sufficiently slow  $\dot{\delta}$  adiabatic loading is achieved.

We perform 3D time-dependent Gross-Pitaevskii equation (TDGPE) calculations to simulate the loading of a BEC from  $|m_F = -1\rangle$  into the dressed state  $|\xi_{-1}\rangle$ . We also solve the absolute ground state using imaginary time propagations at given  $\Omega(r)$  and  $\delta$ .

Our experiment begins with  $N \approx 1.2 \times 10^5$  atoms in a  $^{87}\text{Rb}$  BEC in the  $|F = 1, m_F = -1\rangle$  state in a crossed dipole trap. The TF radius of the condensate is  $R \approx 6.2 \mu\text{m}$  along  $\mathbf{e}_r$ . With a bias magnetic field  $B_0$  along  $\mathbf{e}_x$ , the atoms experience a linear Zeeman shift  $\omega_Z/2\pi = 0.57 \text{ MHz}$  and a quadratic Zeeman shift  $\hbar\omega_q \hat{F}_z^2$  with  $\omega_q/2\pi = 50 \text{ Hz}$ . A Gaussian Raman beam (G) and a Laguerre-Gaussian Raman beam (LG) with phase winding  $m_\ell = 1$  co-propagate along  $\mathbf{e}_z$ , coupling atoms in the  $F = 1$  manifold and transferring OAM of  $\Delta\ell = \hbar$  to the atoms (Fig. 1b). The two Raman laser beams have wavelengths  $\lambda = 790 \text{ nm}$  with a frequency difference  $\Delta\omega_L$  and a Raman detuning  $\delta = \Delta\omega_L - \omega_Z$  (Fig. 1ab). We adiabatically load the BEC into the lowest energy dressed state  $|\xi_{-1}\rangle$  with final Raman coupling strength  $\Omega(r) = \Omega_M \sqrt{e} (r/r_M) e^{-r^2/2r_M^2}$ . Here,  $\Omega_M/2\pi = 3.0 \text{ kHz}$  and  $r_M = 17 \mu\text{m}$  is the peak intensity radius.

The adiabatic loading is achieved by first turning on  $\Omega(r)$  in 7 ms while holding the detuning at  $\delta/2\pi = \delta_f/2\pi + 1.25 \text{ kHz}$ . Next, we sweep the detuning to the final value  $\delta_f$  in 7 ms where  $-500 \text{ Hz} < \delta_f/2\pi < 500 \text{ Hz}$ . After preparing the atoms in the dressed state and holding for a time  $t_h$ , we probe the atoms by switching off the Raman beams and dipole trap simultaneously. After

a 24 ms time-of-flight (TOF) with all  $|m_F\rangle$  components expanding together, we take absorption images along  $\mathbf{e}_z$  for each  $m_F$  states. Images with different final detuning  $\delta$  and  $t_h = 1 \text{ ms}$  are shown in Fig. 2a. For  $\delta > 0$ , the  $|m_F = -1\rangle$  component has no hole, and  $|0\rangle$  carries a smaller hole than that of  $|1\rangle$ , consistent with the fact that  $|-1\rangle, |0\rangle, |1\rangle$  have angular momenta of  $0, \hbar, 2\hbar$ , respectively. The radial cross sections of the spin texture  $D_{m_F}/(D_1 + D_0 + D_{-1})$  are shown (Fig. 2b), which average over the azimuthal angles. Here,  $D_{m_F}$  is the optical density of  $|m_F\rangle$ . We compare these spin textures with the local dressed state  $|\xi_{-1}\rangle$  in Eq. (5) and TOF simulations from TDGPE. The TDGPE simulation gives an  $r_c \approx 1.8 \mu\text{m}$  at  $\delta = 0$ , corresponding to the spin texture agreeing with Eq. (5) at  $r_{\text{TOF}} \gtrsim 23 \mu\text{m}$ .

We further study the stability of the lowest energy dressed state as we hold the Raman field for a variable time  $t_h$ . With a deloading procedure [14] which maps the dressed states  $|\xi_{-1}\rangle, |\xi_0\rangle, |\xi_1\rangle$  back to the bare spin states  $|-1\rangle, |0\rangle, |+1\rangle$ , we measure the population in  $|\xi_n\rangle$  versus  $t_h$ . We take images along  $\mathbf{e}_y$  after 14 ms-TOF with Stern-Gerlach gradient at a variable  $\delta$  with a  $t_h$  up to 7.0 s. Fig. 3a shows the atom number fraction in  $|\xi_n\rangle$  over the total number  $|\xi_{-1}\rangle + |\xi_0\rangle + |\xi_1\rangle$  at  $\delta = 0$  versus  $t_h$ . The atoms slowly populate the excited dressed states  $|\xi_0\rangle$  and  $|\xi_1\rangle$ , and the initial rates increase as the peak Raman coupling is reduced from  $\Omega_M/2\pi = 3.0 \text{ kHz}$  to 1.5 kHz. The lifetime of atom number fraction in  $|\xi_{-1}\rangle$  dropping to 50 % is 4.5 s (1.5 s) for  $\Omega_M/2\pi = 3.0$  (1.5) kHz. Fig. 3b displays the atom number fraction versus detuning at  $t_h = 1 \text{ s}$  and  $\Omega_M/2\pi = 3.0 \text{ kHz}$ , where the population transfer rates decrease with increasing  $|\delta|$ . The results suggest the population transfer rate into excited states increases with a reduction of energy gap  $\approx \sqrt{\Omega(r)^2 + \delta^2}$ ,

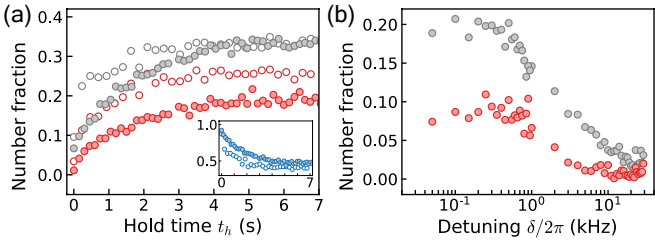


FIG. 3: Stability of lowest energy dressed state  $|\xi_{-1}\rangle$ , shown as the number fraction in the excited dressed states  $|\xi_0\rangle$  (gray symbols) and  $|\xi_1\rangle$  (red symbols): (a) versus hold time  $t_h$  at  $\delta = 0$  for  $\Omega_M/2\pi = 3.0$  kHz (solid symbols) and  $1.5$  kHz (open symbols). Inset shows the number fraction in  $|\xi_{-1}\rangle$  versus  $t_h$ . (b) versus detuning with  $t_h = 1$  s and  $\Omega_M/2\pi = 3.0$  kHz.

which can be explained by the effects of thermal atoms. Our estimated temperature  $T \gtrsim 50$  nK  $\approx h \times 1$  kHz/ $k_B$  is comparable to the energy gap in the experiment. Finally we demonstrate the Hess-Fairbank effect by studying the absolute ground state of dressed atoms in the gauge fields. We begin with thermal atoms right above the BEC transition temperature, load to the lowest energy dressed state with detuning  $\delta$ , and evaporatively cool the atoms to BEC. After a hold time  $t_{h1}$  for free evaporation, we probe the atoms after a 24 ms TOF. We note that there is a different, but related experiment [47], where thermal bosonic atoms are evaporatively spun up and cooled to reach condensation [54].

Similar to the Meissner effect, we tune the synthetic magnetic flux via the detuning  $\delta$  and observe the atoms in the absolute ground state transit from having one quantum number to another. GPE simulations show that the ground states are coreless vortices with  $\ell_g = \pm\hbar$  at  $|\delta|/2\pi > 210$  Hz and are polar-core vortices with  $\ell_g = 0$  at  $|\delta|/2\pi < 210$  Hz (Fig. 4a);  $\ell_g$  is  $\ell$  of the ground state. We obtain the averaged absolute value of winding number  $\langle |\ell_g| \rangle/\hbar$  versus detuning in Fig. 4, by taking TOF images of the bare spin component  $|m_F = 0\rangle$ , whose mechanical angular momentum is  $\ell_g$  under the gauge in Eq. (3). At each  $\delta$  we repeat the experiment for 20 times, observing  $|m_F = 0\rangle$  has either no hole or a hole, indicating  $\ell_g = 0$  or  $\ell_g = \pm\hbar$ , respectively. Such variations are due to the presence of a root-mean-square (rms) detuning noise of  $\approx h \times 70$  Hz (as we repeat the experiment with the same  $t_{h1}$ , see supplement) arising from the bias field noise in our setup. The curve  $\langle |\ell_g| \rangle$  vs.  $\delta/2\pi$  is broadened and can become slightly asymmetric at  $\pm\delta$  since the detuning can slowly vary during the time when the data is taken. A simulation including a Gaussian-distributed detuning noise of  $h \times 70$  Hz rms is plotted in Fig. 4a, with a center shift of -70 Hz. The observed ground state with small  $|\delta|$  has  $\langle |\ell_g| \rangle/\hbar \sim 0$ , corresponding to  $\ell_g = 0$  if there were no detuning noise. Fig. 4a shows the image of the  $\ell_g = 0$  ( $\ell_g = \hbar$ ) dressed state at  $\delta/2\pi = 50$  (400) Hz; the spin textures are schematically drawn in Fig. 4b.

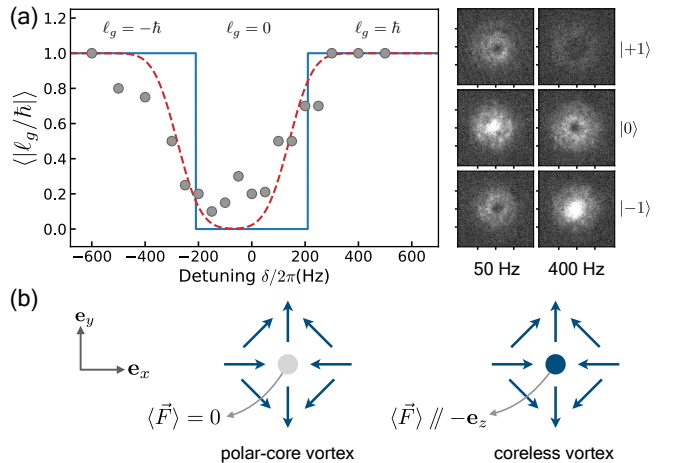


FIG. 4: (a) Transition between  $\ell = 0$  and  $\ell = \pm\hbar$  states in the ground state. The measured average of magnitude of the quasi-angular momentum of the ground state atoms  $\langle |\ell_g| \rangle$  versus detuning  $\delta/2\pi$  (circles) with  $t_{h1} \approx 0.2$  s. At small (large)  $|\delta|$  the ground state has  $|\ell_g| = 0$  ( $\hbar$ ). Examples at  $\delta/2\pi = 50$  and  $400$  Hz are shown with the dressed states' bare spin components taken after TOF. The calculation for the ideal case (solid line) and a simulation including detuning noise in the experiment (dashed-line) are displayed; see text. (b) Schematic drawing of the spin textures at  $\delta > 0$ , where the arrows show the direction of the transverse spin ( $\langle F_x \rangle, \langle F_y \rangle$ ).

We compare our dressed atoms under gauge-induced rotations to BECs under mechanical rotations [48–50]. In Refs. [48–50], Bose-condensation is followed by mechanical stirring. The observed critical rotational angular frequency for single-vortex nucleation is related to dynamical instabilities, and is larger than the critical value  $\omega_c$  for the thermodynamic ground state to possess a single vortex. By contrast, in our demonstration of the Hess-Fairbank effect, the thermal atoms are subjected to the effective rotation and then cooled to BEC in the thermodynamic ground state. Using the gauges in Eq. (4), the synthetic magnetic flux enclosed by the BEC's radius  $R$  is  $\Phi_{B^*}^\pm = h[\cos\beta(R) \mp 1]$ . Fig. 1d shows  $|\Phi_{B^*}^\pm|$  approaches zero at large  $|\delta|$ , and  $\vec{B}^*$  is along  $-(+)\mathbf{e}_z$  at  $\delta > (<) 0$ . Thus, our system is analogous to the transition from zero to single-vortex ground state in rotating BECs as the following:  $\ell^+ = 0 \rightarrow \ell^+ = -\hbar$  (i.e.,  $\ell = \hbar \rightarrow \ell = 0$ ) under  $\Phi_{B^*}^+ < 0$ . And similarly for  $\ell^- = 0 \rightarrow \ell^- = \hbar$  (i.e.,  $\ell = -\hbar \rightarrow \ell = 0$ ) under  $\Phi_{B^*}^- > 0$ . At the transition of  $\delta/2\pi = \pm 210$  Hz,  $|\Phi_{B^*}^\pm| = 0.8$   $h$  is smaller than the critical effective flux  $\Phi_{\text{mech}} = 2\pi m\omega R^2 = h(\omega/\omega_c) \ln(R/r_v)$ , where  $\omega$  is the angular frequency,  $\omega_c = \hbar/(mR^2) \ln(R/r_v)$  [51], and  $r_v$  is the vortex core size. Thus the critical flux is  $\Phi_{\text{mech}}/h > 1$ , while the critical flux for our dressed state is  $|\Phi_{B^*}^\pm|/h < 1$ . This is due to the different form of  $A(r)$  between our dressed atoms and the mechanically rotating BECs (with sym-

metric gauge); see supplement and a similar calculation in Ref. [52].

In conclusion, we demonstrate Raman-coupling-induced azimuthal gauge potentials. They act as effective rotations which we exploit to show Hess-Fairbank effect for the cold atoms. This work paves the way to probe atomic superfluids with effective rotations, which can achieve a stationary Hamiltonian and thermal equilibrium. This scheme circumvents the issues from imperfect cylindrical symmetries in mechanical rotations.

We thank W. D. Phillips, C. Chin and K.-Y. Lin for useful discussions, and Y.-C. Chen and J.-P. Wang for critical readings of our manuscript. Y. J. L acknowledges the support of Career Development Awards in Academia Sinica. S. -K. Y. was supported by MOST. Y. K. was supported by JSPS KAKENHI JP15K17726. M. -S. C. and M. -J. T. were supported by MOST 106-2112-M-001-033.

*Note added:* After we completed the manuscript, we noticed a recent work [53] on pseudo-spin 1/2 SOAMC BECs. They reported observations similar to our demonstration of Hess-Fairbank effect. Our work focuses on the perspective of effective rotations enabled by light-induced azimuthal gauge potentials and characterizing topological spin textures.

- 
- \* Electronic address: linyj@gate.sinica.edu.tw
- [1] Y.-J. Lin, R. L. Compton, A. R. Perry, W. D. Phillips, J. V. Porto, and I. B. Spielman, Phys. Rev. Lett. **102**, 130401 (2009).
  - [2] M. Aidelsburger, M. Atala, M. Lohse, J. T. Barreiro, B. Paredes, and I. Bloch, Phys. Rev. Lett. **111**, 185301 (2013).
  - [3] H. Miyake, G. A. Siviloglou, C. J. Kennedy, W. C. Burton, and W. Ketterle, Phys. Rev. Lett. **111**, 185302 (2013).
  - [4] J. Struck, C. Ölschläger, M. Weinberg, P. Hauke, J. Simonet, A. Eckardt, M. Lewenstein, K. Sengstock, and P. Windpassinger, Phys. Rev. Lett. **108**, 225304 (2012).
  - [5] C. V. Parker, L.-C. Ha, and C. Chin, Nature Physics **9**, 769 (2013).
  - [6] G. Jotzu, M. Messer, R. Desbuquois, M. Lebrat, T. Uehlinger, D. Greif, and T. Esslinger, Nature **515**, 237 (2014).
  - [7] J. Dalibard, F. Gerbier, G. Juzeliūnas, and P. Öhberg, Rev. Mod. Phys. **83**, 1523 (2011).
  - [8] N. Goldman, G. Juzeliūnas, P. Öhberg, and I. B. Spielman, Rep. Prog. Phys. **77**, 126401 (2014).
  - [9] H. Zhai, Reports on Progress in Physics **78**, 026001 (2015).
  - [10] Y. J. Lin, K. Jimenez-Garcia, and I. B. Spielman, Nature **471**, 83 (2011).
  - [11] Z. Wu, L. Zhang, W. Sun, X.-T. Xu, B.-Z. Wang, S.-C. Ji, Y. Deng, S. Chen, X.-J. Liu, and J.-W. Pan, Science **354**, 83 (2016).
  - [12] L. Huang, Z. Meng, P. Wang, P. Peng, S.-L. Zhang, L. Chen, D. Li, Q. Zhou, and J. Zhang, Nature Physics **12**, 540 (2016).
  - [13] G. Juzeliūnas, P. Öhberg, J. Ruseckas, and A. Klein, Physical Review A **71**, 053614 (2005).
  - [14] H.-R. Chen, K.-Y. Lin, P.-K. Chen, N.-C. Chiu, J.-B. Wang, C.-A. Chen, P.-P. Huang, S.-K. Yip, Y. Kawaguchi, and Y.-J. Lin, Physical Review Letters **121**, 113204 (2018).
  - [15] C. Qu, K. Sun, and C. Zhang, Physical Review A **91**, 053630 (2015).
  - [16] M. DeMarco and H. Pu, Physical Review A **91**, 033630 (2015).
  - [17] Y.-X. Hu, C. Miniatura, and B. Grémaud, Physical Review A **92**, 033615 (2015).
  - [18] L. Chen, H. Pu, and Y. Zhang, Physical Review A **93**, 013629 (2016).
  - [19] A. Ramanathan, K. C. Wright, S. R. Muniz, M. Zelan, W. T. Hill, C. J. Lobb, K. Helmerson, W. D. Phillips, and G. K. Campbell, Physical Review Letters **106**, 130401 (2011).
  - [20] S. Beattie, S. Moulder, R. J. Fletcher, and Z. Hadzibabic, Physical Review Letters **110**, 025301 (2013).
  - [21] K. C. Wright, R. B. Blakestad, C. J. Lobb, W. D. Phillips, and G. K. Campbell, Physical Review Letters **110**, 025302 (2013).
  - [22] N. R. Cooper and Z. Hadzibabic, Physical Review Letters **104**, 030401 (2010).
  - [23] A. J. Leggett, Reviews of Modern Physics **71**, S318 (1999).
  - [24] A. J. Leggett, Reviews of Modern Physics **73**, 307 (2001).
  - [25] G. B. Hess and W. M. Fairbank, Physical Review Letters **19**, 216 (1967).
  - [26] R. Ishiguro, O. Ishikawa, M. Yamashita, Y. Sasaki, K. Fukuda, M. Kubota, H. Ishimoto, R. E. Packard, T. Takagi, T. Ohmi, et al., Physical Review Letters **93**, 125301 (2004).
  - [27] S. Moulder, Ph.D. thesis, University of Cambridge (2013).
  - [28] Y. Kawaguchi and M. Ueda, Physics Reports **520**, 253 (2012).
  - [29] M. Ueda, Reports on Progress in Physics **77** (2014).
  - [30] T. Isoshima, M. Nakahara, T. Ohmi, and K. Machida, Physical Review A **61**, 063610 (2000).
  - [31] A. E. Leanhardt, Y. Shin, D. Kielpinski, D. E. Pritchard, and W. Ketterle, Physical Review Letters **90**, 140403 (2003).
  - [32] M. W. Ray, E. Ruokokoski, S. Kandel, M. Möttönen, and D. S. Hall, Nature **505**, 657 (2014).
  - [33] M. W. Ray, E. Ruokokoski, K. Tiurev, M. Möttönen, and D. S. Hall, Science **348**, 544 (2015).
  - [34] D. S. Hall, M. W. Ray, K. Tiurev, E. Ruokokoski, A. H. Gheorghe, and M. Möttönen, Nature Physics **12**, 478 (2016).
  - [35] T. Ollikainen, K. Tiurev, A. Blinova, W. Lee, D. Hall, and M. Möttönen, Physical Review X **7**, 021023 (2017).
  - [36] J.-Y. Choi, W. J. Kwon, and Y.-I. Shin, Physical Review Letters **108**, 035301 (2012).
  - [37] J.-Y. Choi, W. J. Kwon, M. Lee, H. Jeong, K. An, and Y.-i. Shin, New Journal of Physics **14**, 053013 (2012).
  - [38] W. Lee, A. H. Gheorghe, K. Tiurev, T. Ollikainen, M. Möttönen, and D. S. Hall, Science Advances **4**, eaao3820 (2018).
  - [39] J.-Y. Choi, S. Kang, S. W. Seo, W. J. Kwon, and Y.-i. Shin, Physical Review Letters **111**, 245301 (2013).
  - [40] L. S. Leslie, A. Hansen, K. C. Wright, B. M. Deutscher, and N. P. Bigelow, Physical Review Letters **103**, 250401

- (2009).
- [41] A. Hansen, Ph.D. thesis, University of Rochester (2016).
- [42] T. Isoshima, K. Machida, and T. Ohmi, Journal of the Physical Society of Japan **70**, 1604 (2001).
- [43] L. E. Sadler, J. M. Higbie, S. R. Leslie, M. Vengalattore, and D. M. Stamper-Kurn, Nature **443**, 312 (2006).
- [44] T.-L. Ho, Physical Review Letters **81**, 742 (1998).
- [45] T.-L. Ho and V. B. Shenoy, Physical Review Letters **77**, 2595 (1996).
- [46] Y. Castin and R. Dum, Physical Review Letters **77**, 5315 (1996).
- [47] P. C. Haljan, I. Coddington, P. Engels, and E. A. Cornell, Physical Review Letters **87**, 210403 (2001).
- [48] K. W. Madison, F. Chevy, V. Bretin, and J. Dalibard, Phys. Rev. Lett. **86**, 4443 (2001).
- [49] J. R. Abo-Shaeer, C. Raman, J. M. Vogels, and W. Ketterle, Science **292**, 476 (2001).
- [50] E. Hodby, G. Hechenblaikner, S. A. Hopkins, O. M. Maragò, and C. J. Foot, Physical Review Letters **88**, 010405 (2001).
- [51] E. Lundh, C. J. Pethick, and H. Smith, Physical Review A **55**, 2126 (1997).
- [52] G. Juzeliunas and P. Öhberg, Optics and Spectroscopy **99**, 357 (2005).
- [53] D. Zhang, T. Gao, P. Zou, L. Kong, R. Li, X. Shen, X.-L. Chen, S.-G. Peng, M. Zhan, H. Pu, et al. (2018), arXiv:1806.06263.
- [54] In Ref. [47], they study vortex nucleation into a BEC in the environment of rotating thermal atoms.
-

## Supplemental Materials: Rotating atomic quantum gases with light-induced azimuthal gauge potentials and the observation of the Hess-Fairbank effect

### TDGPE SIMULATIONS

We numerically simulate the dynamics by solving the three-component 3D time-dependent-Gross-Pitaevskii equation (TDGPE). This includes the kinetic energies, quadratic Zeeman energy, mean field interaction parameters  $c_0 = 4\pi\hbar^2(a_0 + 2a_2)/3m$  and  $c_2 = 4\pi\hbar^2(a_2 - a_0)/3m < 0$ , where  $a_f$  is the s-wave scattering length in the total spin  $f$  channel [S3].

We use the Crank-Nicolson method and calculate in the system size of  $(256)^3$  grid points with grid size  $0.16 \mu\text{m}$ . During TOF, we solve the full 3D TDGPE for up to  $\leq 4$  ms at which the interatomic interaction energy becomes less than 3 percent of the total energy. The further evolution is calculated by neglecting the interaction term. The results for the lowest energy dressed state with a short hold time  $t_h = 1$  ms are shown in Fig. S1; our corresponding data is in Fig. 2. Using the loaded atomic state from TDGPE at  $\delta = 0$ , the probability of projection to the local dressed state  $|\xi_{-1}\rangle$  is  $\geq 0.99$  at  $r \geq r_c = 1.8 \mu\text{m}$ .

### SYNTHETIC MAGNETIC FLUX OF DRESSED ATOMS

We compare the thermodynamic ground state of the dressed atoms in  $|\xi_{-1}\rangle$  under synthetic magnetic fields to that of mechanically rotating BECs. Taking  $\delta > 0$  where  $\vec{B}^* \cdot \mathbf{e}_z < 0$  as the example, we consider the azimuthal kinetic energy in Eq. (1), which is gauge invariant and can be written as  $(\ell^+ - rA_{-1}^+)^2/2mr^2$  in the gauge of Eq. (4). Here we simplify the calculation by assuming a disk BEC geometry, although our BEC is 3D and has a Thomas-Fermi (TF) profile. Similar calculations for 3D TF BECs are shown in Ref. [S4]. The contribution to the kinetic energy per atom is

$$\begin{aligned} & \frac{1}{\pi R^2} \int_0^R dr 2\pi r \frac{(\ell^+ - rA_{-1}^+)^2}{2mr^2} \\ &= \frac{1}{\pi R^2} \left[ \int dr 2\pi r \frac{(\ell^+)^2}{2mr^2} - \int dr 2\pi r \frac{\ell^+ \hbar}{mr^2} (\cos \beta - 1) + \int dr 2\pi r \frac{(rA_{-1}^+)^2}{2mr^2} \right]. \end{aligned} \quad (\text{S1})$$

With  $\delta > 0$ ,  $\cos \beta - 1$  is negative. We thus compare the energy with  $\ell^+ = 0$  and with  $\ell^+ = -\hbar$ , where the lower one is the ground state. The energy for  $\ell^+ = -\hbar$  relative to  $\ell^+ = 0$  is

$$E_{B^*} = \frac{1}{\pi R^2} \int_{r_v}^R dr 2\pi r \frac{\hbar^2}{2mr^2} + \frac{1}{\pi R^2} \int_0^R dr 2\pi r \frac{\hbar^2}{mr^2} (\cos \beta - 1), \quad (\text{S2})$$

where the first term is the vortex kinetic energy  $E_v$  and  $r_v$  is the vortex core size. At large  $\delta$ ,  $\cos \beta - 1 \approx 0$  and  $E_{B^*} \approx E_v$ , leading to the  $\ell^+ = 0$  ground state. As  $\delta$  decreases,  $|\cos \beta - 1|$  increases, and the ground state makes a transition to  $\ell^+ = -\hbar$  when the absolute value of the second term in Eq. (S2) equals  $E_v$ .

Then we analogously consider a mechanically rotating BEC with angular frequency  $-\omega$ , where  $\omega > 0$ . The kinetic energy for  $\ell = -\hbar$  relative to  $\ell = 0$  is

$$\begin{aligned} E_{\text{mech}} &= \frac{1}{\pi R^2} \int_{r_v}^R dr 2\pi r \frac{\hbar^2}{2mr^2} - \frac{1}{\pi R^2} \int_0^R dr 2\pi r \frac{\hbar^2}{mr^2} \frac{m\omega r^2}{\hbar} \\ &= E_v - \frac{1}{\pi R^2} \int_0^R dr 2\pi r \hbar \omega. \end{aligned} \quad (\text{S3})$$

The critical angular frequency for the ground state changes from  $\ell^+ = 0$  to  $\ell^+ = -\hbar$  with increasing  $\omega$  is  $\omega_c = \hbar/(mR^2) \ln(R/r_v)$ .

To compare the dressed atoms and the mechanically rotating BEC, we consider the dimensionless gauge potential  $rA/\hbar$ , which is equal to the flux  $\Phi$  enclosed by radius  $r$  in unit of  $\hbar$ , given that  $\oint \vec{A} \cdot d\vec{l} = A(r)2\pi r = \Phi$ ;  $\Phi$  represents  $\Phi_{B^*}^+$  and  $\Phi_{\text{mech}}$ . We then plot  $rA_{-1}^+/\hbar = \cos \beta(r) - 1$  and  $m\omega_c r^2/\hbar$  versus  $r$  in Fig. S2a, showing curves of  $\cos \beta(r) - 1$  with various detuning  $\delta/2\pi$  for the dressed atoms. Here we use  $r_v = 0.5 \mu\text{m}$  for both Eq. (S2) and Eq. (S3), and thus  $\omega_c/2\pi = 8.0 \text{ Hz}$  for the TF radius  $R \approx 6 \mu\text{m}$ . We derive  $r_v$  for dressed atoms from the projection probability of the

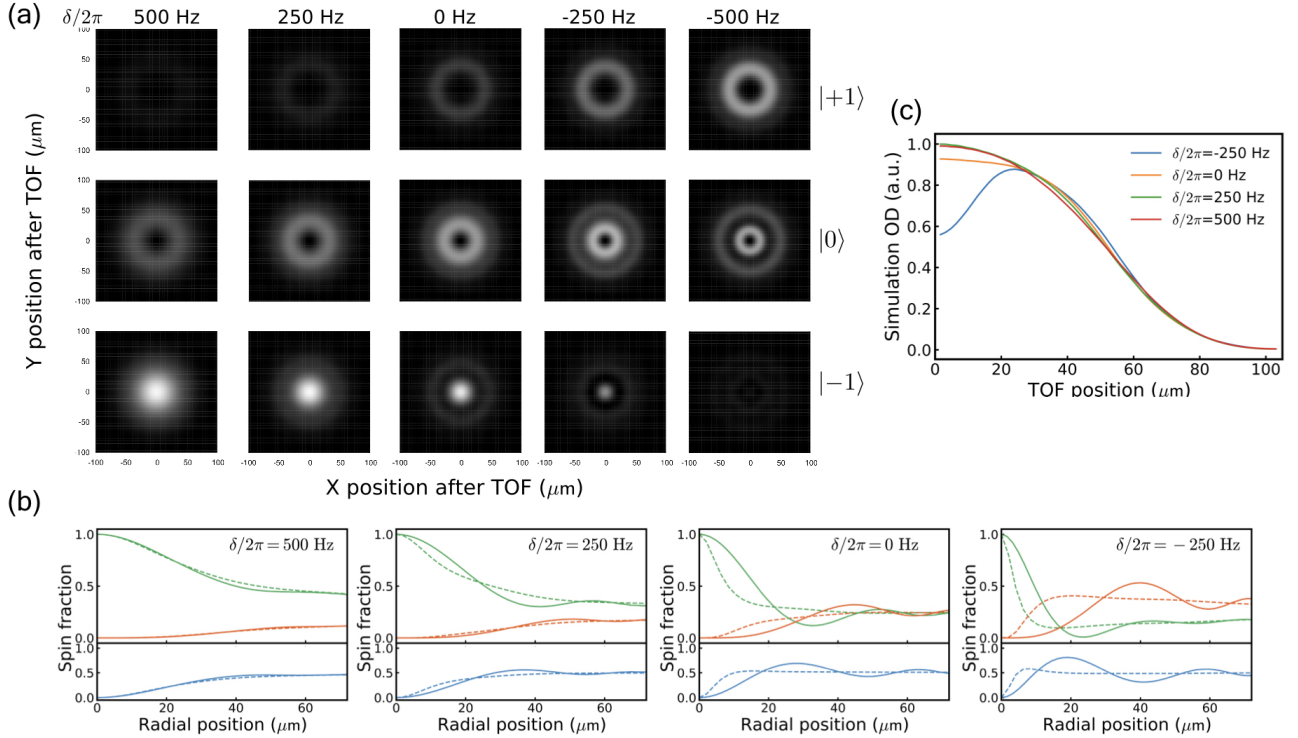


FIG. S1: 3D TDGPE simulation results for the BEC loaded into the  $\ell = \hbar$  lowest energy dressed state at various detuning  $\delta$  with a hold time  $t_h = 1 \text{ ms}$ . (a) Absorption images  $D_{m_F}$  after a 24 ms TOF. The image field of view is  $200 \times 200 \mu\text{m}$ . (b) Spin texture  $D_{m_F}/(D_1 + D_0 + D_{-1})$  vs. radial position. Dashed curves denote the in-situ profile after a  $r \rightarrow r/13.0$  magnification; solid curves denote those after a 24 ms TOF. Green, orange and blue curves denote  $| -1\rangle$ ,  $| +1\rangle$ ,  $| 0\rangle$ , respectively. (c) total optical density ( $D_1 + D_0 + D_{-1}$ ) for simulated TOF profiles.

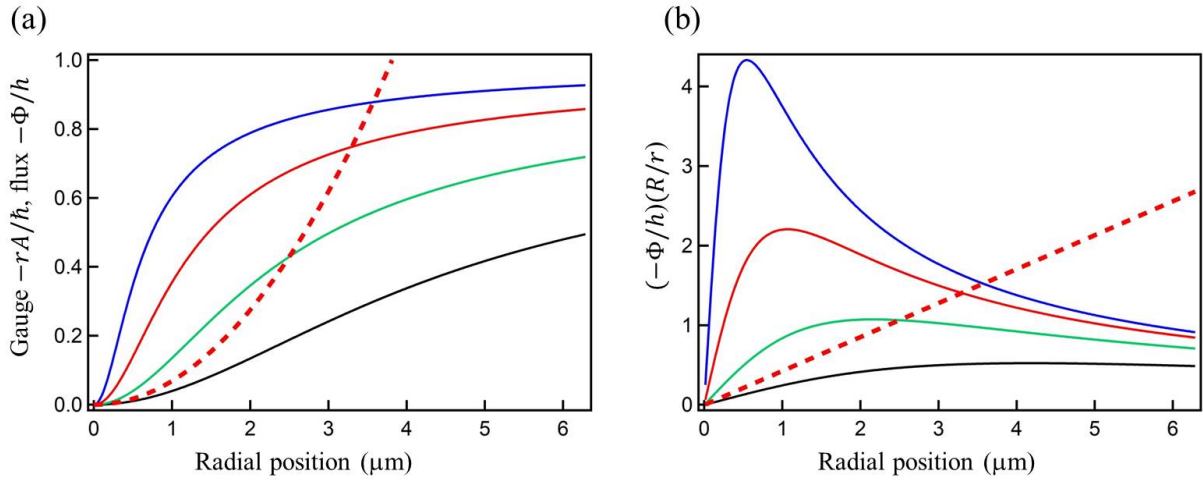


FIG. S2: (a) Gauge potential  $-rA_{-1}^+/h$ , which is equal to the flux  $-\Phi/h$ , versus radial position  $r$ . Black, green, red and blue solid curves denote the lowest energy dressed state with  $\delta/2\pi = 1000, 500, 295, 125 \text{ Hz}$ , respectively.  $\delta_c/2\pi = 295 \text{ Hz}$  is the critical detuning. Red dashed curve represents the mechanically rotating BEC with the critical frequency  $\omega_c$ . (b)  $-(\Phi/h)(R/r)$  versus  $r$ . Symbols represent the same as those in (a).

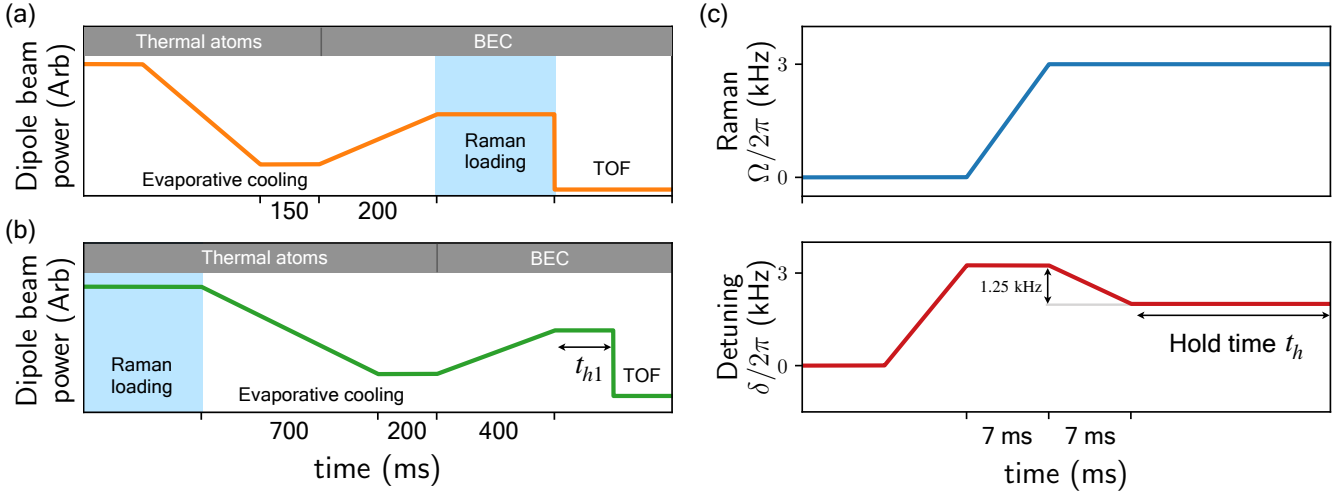


FIG. S3: Time sequences of the experiment. (a) Dipole beam power in the procedure for the coreless vortex data in Fig. 2. (b) Dipole beam power in the procedure for data in Fig. 4 showing Hess-Fairbank effect. (c) The sequences of Raman loading in (a) and (b).

spinor wave function of the absolute ground state with  $\ell^+ = -\hbar$  (i.e.,  $\ell = 0$ ) onto  $|\xi_{-1}\rangle$ , where Eq. (S1) applies. This probability is zero at  $r = 0$  and increases with increasing  $r$ , and we take  $r_v$  as the radial position with the probability of 0.65. We find  $r_v \sim 0.5 \mu\text{m}$  is approximately independent of  $\delta$  for  $125 \text{ Hz} < \delta/2\pi < 300 \text{ Hz}$ .

From Fig. S2a, we observe the flux enclosed by  $r = R$  is  $|\Phi_{\text{mech}}|/h \approx 2.6 > 1$  while  $|\Phi_{B^*}^+|/h < 1$  is limited by our  $\Delta\ell = \hbar$ . Since  $E_v$  is the same in Eq. (S2) and Eq. (S3), we then compare the integrand of the second term in Eq. (S2) and Eq. (S3), respectively, versus  $r$  in Fig. S2b, which are contributed from the gauge potential  $rA_{-1}^+$  and  $m\omega_c r^2$ . The integrand is scaled as  $(\Phi/h)(R/r)$ . At the critical detuning  $\delta_c$  for the dressed atoms, the quasi-angular momentum  $\ell^+ = \ell - \hbar$  of the ground state changes from 0 to  $-\hbar$ . We determine  $\delta_c$  from Fig. S2b, where the enclosed area by the red curve denoting  $\delta_c$  equals to that of the red-dashed curve representing the mechanically rotating BEC with the critical frequency  $\omega_c$ . We find this condition is fulfilled at  $\delta_c/2\pi \approx 295 \text{ Hz}$ . Fig. S2a shows that at small  $r$  the gauge potential  $|rA_{-1}|$  of dressed atoms with  $\delta/2\pi \leq 500 \text{ Hz}$  is larger than the  $m\omega_c r^2$  for the mechanical rotation; the contribution at small  $r$  is further enhanced by the  $2\pi\hbar^2/(mr)$  factor in the integrand (see Fig. S2b). Therefore, the critical flux for the symmetric gauge is  $|\Phi_{\text{mech}}|/h > 1$  while  $|\Phi_{B^*}^+|/h \approx 0.8 < 1$  for our dressed atoms.

## EXPERIMENTAL SETUP AND PROCEDURES

For the coreless vortex data in Fig. 2, we first produce a  $^{87}\text{Rb}$  BEC and then load it into the Raman-dressed state  $|\xi_{-1}\rangle$ . We achieve a BEC of  $N \approx 1.2 \times 10^5$  atoms in a crossed dipole trap in  $|F, m_F\rangle = |1, -1\rangle$  [S1]. The dipole trap contains two 1064 nm laser beams propagating along  $\mathbf{e}_{x'}, \mathbf{e}_{y'} = (\mathbf{e}_x \pm \mathbf{e}_y)/\sqrt{2}$  with beam waists of  $\sim 30 \mu\text{m}$ . After the forced evaporation and a 1.5 s free evaporation, the dipole beam powers are ramped up in 0.2 s in order to reach the final trap frequencies of  $(\omega_x', \omega_y', \omega_z)/2\pi = (140, 140, 190) \text{ Hz}$ . The radial trap frequency is chosen such that it is sufficient for the atoms to sustain a Thomas-Fermi profile in the presence of the anti-trapping light shift potential near Raman resonance,  $-\sqrt{\Omega(r)^2 + \delta^2}$ .

After the BEC preparation we wait for the external trigger from the 60 Hz line, after which we apply feed-forward current signals into bias coils to cancel the field noise from 60 Hz harmonics (see later discussions). Then we load the  $|m_F = -1\rangle$  BEC into the lowest energy dressed state  $|\xi_{-1}\rangle$  with the following procedures. We ramp the detuning to  $\delta/2\pi = \delta_f/2\pi + 1.25 \text{ kHz}$  while the Raman beams are off, ramp  $\Omega(r, t)$  in 7 ms to the final value of  $\Omega_M/2\pi = 3.0 \text{ kHz}$ , and then ramp the detuning to  $\delta_f/2\pi$  between 500 Hz and -500 Hz in 7 ms (see Fig. S3), subsequently holding  $\Omega_M$  and  $\delta$  at constant for  $t_h$ . The Raman beams are at  $\lambda = 790 \text{ nm}$  where their scalar light shifts from the D1 and D2 lines cancel. The Gaussian Raman beam has a waist of  $200 \mu\text{m}$ , and the LG Raman beam produced by a vortex phase plate has a phase winding number  $m_\ell = 1$  and radial index of 0. The Raman beams are linearly polarized along  $\mathbf{e}_x$  and  $\mathbf{e}_y$ , respectively.

To show the Hess-Fairbank effect in Fig. 4, we start with thermal atoms right above the BEC transition temperature, load to the dressed state  $|\xi_{-1}\rangle$  using the same sequence as that for data in Fig. 2. Next we force evaporatively cool

the atoms to achieve BECs and hold 0.2 s for free evaporation, then increase the dipole beam powers in 0.4 s to reach the trap frequencies ( $\omega_x', \omega_y', \omega_z$ ), subsequently holding for  $t_{h1}$  before TOF. To reduce the shot-to-shot field noise when TOF starts, we wait for the 60 Hz line trigger at 20 ms before the TOF. This adds to  $t_{h1}$  by a varying time up to 16.7 ms (period of 60 Hz) as the experiment is repeated.

For projection measurements of the spinor state  $|\xi_s\rangle$ , we abruptly turn off the dipole trap and Raman beams, simultaneously and adiabatically rotate the magnetic bias field from along  $\mathbf{e}_x$  to that along the imaging beam direction within 0.4 ms. The spinor wave function is then projected to the bare spin  $m_F$  basis. For data in Fig. 2 and Fig. 4, the atoms then expand in free space with all  $m_F$  components together for a TOF. To perform spin-selective imaging, we apply microwave spectroscopy for imaging each  $|m_F\rangle$  [S1]. Each  $|m_F\rangle$  image is obtained in an individual experimental realization. After the  $F = 1$  atoms are transferred to  $F = 2$  by the microwave pulses, we apply a resonant absorption imaging pulse of  $\sim 14 \mu\text{s}$  with  $\sigma+$  polarization at the  $|F = 2, m_F = 2\rangle \rightarrow |F' = 3, m_F = 3\rangle$  cycling transition. With our  $I/I_{\text{sat}}$  parameters, we use the modified Beer-Lamberet law [S2] to derive correct optical densities. For data in Fig. 3, we apply a Stern-Gerlach field gradient to spatially separate individual  $|m_F\rangle$  states during TOF, then a  $F = 1 \rightarrow F' = 2$  repumping pulse is applied, after which the images of all  $|m_F\rangle$  states are taken in a single shot.

We characterize the ambient field noise after the external trigger from the 60 Hz line. The noise is dominated by the 60 Hz line signal with a standard deviation ( $\sigma$ ) of  $\sim h \times 300 \text{ Hz}$ . After we apply feed-forward signals in the bias fields to cancel the dominating field noise at 60 Hz, the  $1 - \sigma$  residual field noise can be reduced to  $h \times 120 \text{ Hz}$  within 0.4 s after the 60 Hz trigger, in the best case. For longer time the 60 Hz line has a phase decoherence and the feed-forward cancelation does not work. For the data in Fig. 2 where the Raman loading takes 14 ms, we prepare the dressed state after the 60 Hz line trigger in order to reduce the shot-to-shot field variation with a fixed time after the trigger, and the measured  $1 - \sigma$  field noise from repeated experimental shots is  $\sim h \times 70 \text{ Hz}$ .

## DATA ANALYSIS

For data in Fig. 2, we average over 4 to 5 images for each  $\delta$  taken under identical conditions. We post-select images whose vortex positions in  $|m_F = \pm 1\rangle$  with respect to the BEC center are  $< 0.3 \mu\text{m}$  (converted from TOF position to the in-situ position). We determine  $\delta/2\pi$  from the rf-spectroscopy with an uncertainty of  $\approx 20 \text{ Hz}$ . The uncertainty of the spin fraction displayed in Fig. 2b is  $\sigma/\sqrt{N}$ , where  $\sigma$  is the standard deviation of pixels along  $\mathbf{e}_\phi$  at a fixed  $r$ , and  $N = 4$  or 5 is the number of images.

For data in Fig. 4, the variations in the winding number of  $|m_F = 0\rangle$  component within 20 identical experimental realizations are most likely due to the detuning noise. Thus, in the images at  $\delta/2\pi = 50 \text{ Hz}$  with  $\langle|\ell_g|\rangle/\hbar \sim 0$ , for  $|m_F = 0\rangle$  component we post-select those with no hole corresponding to  $\ell_g = 0$ . For  $|m_F = 1\rangle$  component we select those with smaller holes corresponding to  $\ell_g + \hbar = \hbar$  and excluding those with larger holes corresponding to  $\ell_g + \hbar = 2\hbar$ . Similarly, we post-select those with  $\ell_g - \hbar = -\hbar$  in  $|m_F = -1\rangle$  with  $\delta/2\pi = 50 \text{ Hz}$ , and further select those with  $\ell_g = \hbar$  for  $|m_F = 0, \pm 1\rangle$  images with  $\delta/2\pi = 400 \text{ Hz}$  based on the hole size in the images. For both  $\delta/2\pi = 50, 400 \text{ Hz}$ , each  $m_F$  state image is a single-shot image.

In the Hess-Fairbank effect experiment, we consider the effects of the dominating detuning noise at 60 Hz with an amplitude of  $\approx h \times 420 \text{ Hz}$ . After BEC is reached, the sum of the hold time and the ramp time of dipole beam power is 0.8 s. After the 60 Hz line signal decoheres, the feed-forward cancelation does not function, and thus the 60 Hz detuning noise could drive the atoms slightly out of the equilibrium and out of the absolute ground state. Further reduction of bias field noise is needed in order to improve the current measurements.

---

\* Electronic address: linyj@gate.sinica.edu.tw

- [S1] H. R. Chen, K. Y. Lin, P. K. Chen, N. C. Chiu, J. B. Wang, C. A. Chen, P. P. Huang, S. K. Yip, Y. Kawaguchi, and Y. J. Lin (2018), arXiv:1803.07860.  
[S2] G. Reinaudi, T. Lahaye, Z. Wang, and D. Guéry-Odelin, Optics Letters **32**, 3143 (2007).  
[S3] T.-L. Ho, Physical Review Letters **81**, 742 (1998).  
[S4] E. Lundh, C. J. Pethick, and H. Smith, Physical Review A **55**, 2126 (1997).